# Magnetic-field coils for metastability-exchange optical pumping, spectroscopy, and magnetic resonance of helium

Pierre-Jean Nacher

▶ **To cite this version:**

Pierre-Jean Nacher. Magnetic-field coils for metastability-exchange optical pumping, spectroscopy, and magnetic resonance of helium. Review of Scientific Instruments, 2024, 95 (8), pp.083306. 10.1063/5.0216482 . hal-03243760

**HAL Id: hal-03243760**
**https://hal.science/hal-03243760**

Submitted on 8 Aug 2024

**HAL** is a multi-disciplinary open access archive for the deposit and dissemination of scientific research documents, whether they are published or not. The documents may come from teaching and research institutions in France or abroad, or from public or private research centers.

L'archive ouverte pluridisciplinaire **HAL**, est destinée au dépôt et à la diffusion de documents scientifiques de niveau recherche, publiés ou non, émanant des établissements d'enseignement et de recherche français ou étrangers, des laboratoires publics ou privés.

Distributed under a Creative Commons Attribution - NonCommercial - NoDerivatives 4.0 International License

# Magnetic-field coils for metastability-exchange optical pumping, spectroscopy, and magnetic resonance of helium

Pierre-Jean Nacher*

*Laboratoire Kastler Brossel, ENS-Université PSL, CNRS, Sorbonne Université, Collège de France; 24 rue Lhomond, 75005 Paris, France.*

**Abstract** Optical pumping on the $2^3S$–$2^3P$ transition (1083 nm) of metastable $^3$He or $^4$He atoms is used for science and applications. Gas is usually enclosed in elongated cells with lengths ranging from several centimeters to several meters for efficient absorption. Good magnetic-field homogeneity is needed for weak diffusion-induced relaxation and long NMR signal lifetimes. A compact coil system is designed using a target-oriented numerical optimisation method. It provides a suitably uniform field over cell volumes, with characteristics depending on chosen optimisation parameters. Additional pairs of coils can be used to generate transverse field components with contributions to total field inhomogeneities that are discussed.

## 1 Introduction

Optical pumping (OP) operating on the $2^3S$ metastable state of helium is an efficient method used to achieve high polarisations in low-pressure helium gas. In $^3$He or isotopic mixtures of $^3$He and $^4$He, it yields high nuclear polarisations in the $^3$He ground state via metastability-exchange (ME) collisions, and MEOP is used for a variety of applications.[1] Weak rf discharges are used to sustain a suitable density of metastable atoms, with typical absorption lengths as long as meters, especially at high polarisations. Therefore, long cells or sets of parallel long cells are used to significantly absorb the available laser pumping light and polarise large volumes of gas, that is subsequently compressed by high-yield polarisation-preserving compressors.[2] More compact polarising systems can be designed with shorter OP cells, with smaller volumes better suited to smaller-scale compressors.[3, 4, 5, 6] In all systems, the polarised gas is compressed into a storage volume situated in the vicinity of the OP cell or cells.

A holding magnetic field **B** must be applied along the direction of propagation of the circularly-polarised light beam used for OP. A field magnitude of the order of 1 mT or less is generally used, with a high enough relative homogeneity so as to avoid fast gradient-induced magnetic relaxation of the (longitudinal) nuclear polarisation. The rate of this relaxation can usually be linked with the gradients of the transverse field components $B_x$ and $B_y$ and depends on gas pressure.[7] The average relaxation rate over an extended volume, in which field inhomogeneities may significantly differ from linear variations, may be computed from maps of the local values of $\nabla B_x$ and $\nabla B_y$. Efficient operation of gas polarising systems requires negligible relaxation-induced losses both in the OP cell, in which the low-pressure (∼mbar) gas dwell time is usually of the order of tens to hundreds of seconds, and in the storage volume, in which high-pressure (∼bar) gas may reside for tens to hundreds of minutes. This is typically achieved for relative field inhomogeneities below a few $10^{-3}$/cm in the relevant volumes (see Sect. 2.2 for the evaluation of the targeted inhomogeneities). Additionally, monitoring of the gas magnetisation in the storage volume by pulsed NMR is usually implemented. Long coherence times ($T_2^*$) of NMR precession, needed for sensitive measurements, require a high absolute homogeneity of the longitudinal field component $B_z$, typically better than 100 nT over the storage volume.

Various designs have been described to generate holding fields **B** with suitable homogeneity. Large enough Helmholtz coils[3] or sets of four circular coils (two pairs with different diameters),[6] providing highly uniform fields over spherical volumes, are used in some compact systems. Larger numbers of circular coils or end-compensated solenoids, sometimes combined with magnetic shields, are used for MEOP of very long cells.[2] This article reports on the design and performance of systems of coils providing fields with sufficient uniformity over cylindrical OP cells of intermediate lengths (typically up to 60 cm) and diameters up to 6 cm while retaining as small a footprint as possible. Geometrical constraints and ease of construction are met with coil systems comprising six square coils wound on identical frames, an extension of the schemes of Merritt et al.[8] However, in contrast with usual coil design approaches, performing exact field calculations is preferred here to using Taylor expansions of the field components. Numerical optimisation of coil parameters is performed to minimise suitable cost functions related to necessary field homogeneity over OP and storage volumes. This approach is shown to yield significantly better solutions than the cancellation of low-order field derivatives at the origin which is often used.[8, 9, 10, 11]

This article is organised as follows: Sect. 2 introduces notations to describe the coil systems and perform numerical field computations, then describes the method used for optimisations of field maps. Sect. 3 first describes re-

*nacher@lkb.ens.fr, corresponding author.

sults for simple on-axis optimisation, then for joint optimisations over OP and storage volumes, and additionally discusses the effect of simple Earth's field compensation coils. Illustrative comparisons with characteristics of experimental systems are given. Key results and possible extensions are briefly discussed in Sect. 4

# 2 Coil design

## 2.1 Field map computations

The building block of the field map computations is the integrated Biot–Savart law for a straight current path element. With the notations of Fig. 1a, the field at point P from the current $I$ flowing from $P_1$ to $P_2$ is perpendicular to the plane of the figure and its magnitude is

$$B_{12} = \frac{\mu_0 N I}{4\pi r_\perp} \left(\sin\alpha_2 - \sin\alpha_1\right). \tag{1}$$

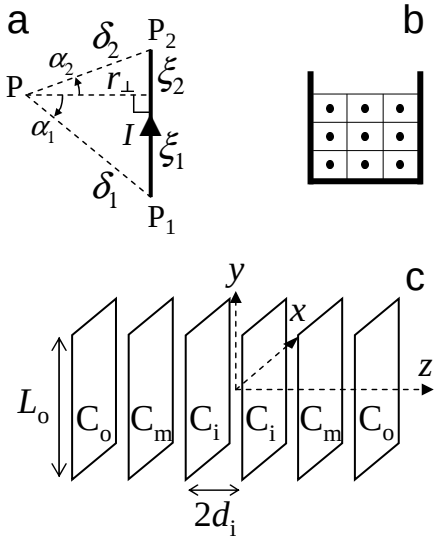


Figure 1: Schematics of current elements generating the magnetic field. a: Geometrical parameters for computing the field magnitude at point P from the current path $P_1 \rightarrow P_2$ (Eq. 1). b: Approximation of an extended winding partly filling a rectangular U-profile, replaced with a lattice of linear currents (here 3×3 elements). c: Three pairs of square coils (inner, median, and outer, $C_i$, $C_m$, and $C_o$) are symmetrically placed along the $z$-axis. Their side lengths ($L$), separations ($2d$), and numbers of turns ($N$, not displayed), carry the index i, m, or o designating the relevant coil pair.

This elementary field magnitude can be expressed in terms of the distances $\delta_j$ between P and $P_j$, $\xi_1$, $\xi_2$ and $L = \xi_1 + \xi_2$ between $P_1$ and $P_2$ (see Fig. 1a) as

$$B_{12} = \frac{\mu_0 N I}{4\pi} \left(\frac{\xi_1}{\delta_1} - \frac{\xi_2}{\delta_2}\right) \left(\delta_1^2 - \xi_1^2\right)^{-1/2}, \tag{2}$$

where the various lengths can be computed from the coordinates of P $(x, y, z)$ and of $P_j$ $(x_j, y_j, z_j;\ j = 1, 2)$:

$$\delta_j = \left[(x_j - x)^2 + (y_j - y)^2 + (z_j - z)^2\right]^{-1/2} \tag{3}$$

$$\xi_j = \left[(x - x_j)(x_2 - x_1) + (y - y_j)(y_2 - y_1) + (z - z_j)(z_2 - z_1)\right]/L. \tag{4}$$

The lengths $\xi_j$ are evaluated from the dot products $\overrightarrow{P_jP}.\overrightarrow{P_1P_2}$ whereas the direction of the field is that of the cross product $\mathbf{\Lambda} = \overrightarrow{P_1P} \times \overrightarrow{P_1P_2}$, with components:

$$\Lambda_x = (z_2 - z_1)(y - y_1) - (y_2 - y_1)(z - z_1), \tag{5}$$

$$\Lambda_y = (x_2 - x_1)(z - z_1) - (z_2 - z_1)(x - x_1), \tag{6}$$

$$\Lambda_z = (y_2 - y_1)(x - x_1) - (x_2 - x_1)(y - y_1). \tag{7}$$

The components of the magnetic field can finally be expressed from those of $\mathbf{\Lambda}$ using

$$\mathbf{B}_{12} = B_{12}\mathbf{\Lambda}\left(\Lambda_x^2 + \Lambda_y^2 + \Lambda_z^2\right)^{-1/2}. \tag{8}$$

Equations 2 to 8 are explicitly used in computer codes to numerically evaluate the magnetic field components $B_x$, $B_y$, and $B_z$ at any point P.

Typical coils comprise tens to hundreds of turns of wire of circular cross section layered inside U-shaped profiles. The detailed distribution of current density in the coil cross-section is not evaluated and the helical winding pattern is overlooked,[11] but instead the field generated by a discrete lattice of $n \times p$ elementary currents inside the winding volume (Fig. 1b) is computed. In practice, $n$ and $p$ range from 1 for a fast coarse approximation to 10 for the most accurate computations.

The coil sets consist of three pairs of square coils arranged as sketched in Fig. 1c. The components of the total field at point P are computed by summing the $24np$ contributions obtained using Eq. 8 for the elementary currents representing each side of each coil. Their expressions involve the common inner side length $L_{\min}$ of the frames, the widths and thicknesses of the windings, the coil spacings, and the number of turns (all coils are connected in series). This summation is numerically performed as well. The typical computation time of one field value is of the order of 1 $\mu$s for $np = 1$ using a standard PC (Intel i7 CPU at 4 GHz, GNU Fortran compiler, –O3 optimisation for speed).

## 2.2 Optimisation of coil parameters

Six parameters are used to characterise the coil system configurations: the three coil half-separations $d_k$ and the three numbers of turns $N_k$. As a coarse approximation, only two ratios of turns, e.g. $N_i/N_o$ and $N_m/N_o$, may strongly influence the field maps and are therefore retained as free parameters for the optimisations besides the values of $d_k$. However, since all $N_k$ are integers in actual systems, the value of $N_o$ is indeed relevant. Moreover, coil

construction details such as the widths and depths of the windings also influence the field maps.

As discussed in introduction, the optimised field map should jointly achieve a high uniformity of all its components over the volume $V_S$ of a storage cell (typically a sphere) and of its transverse components over the volume $V_{OP}$ of the OP cell (long cylinders). The locations of these volumes are sketched in Fig. 2 for two examples of coil systems actually implemented in gas polarising systems (Fig. 3). The construction,, operation, and performance of these polarising systems will be described elsewhere, but selected characterisations of their field homogeneity are reported in Sect. 3.

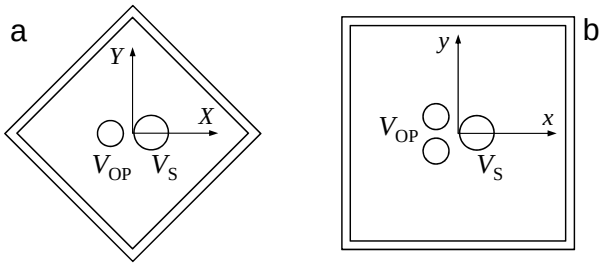


Figure 2: Views in the plane $z = 0$ of the locations of the spherical storage cell $V_S$ and the cylindrical OP cell(s) $V_{OP}$ for two coil sets. a: For the smaller set ($L_{min} = 38.4$ cm) the cells are offset from the coil set center along a diagonal direction $X$: $-5.5$ cm for $V_{OP}$ (I.D. 4.5 cm, length 50 cm) and 4.5 cm for $V_S$ (I.D. 8 cm) b: For the larger set ($L_{min} = 50.4$ cm) the OP volume comprises two cylinders (offsets $-5.2$ cm and $\pm 4$ cm, I.D. 6.1 cm, length 65 cm); $V_S$ offset: 4 cm.

Cost functions defined from computed field maps are used to assess the field uniformity over each volume that is relevant for the targeted application. For the OP volume $V_{OP}$, two averages over $V_{OP}$ are considered, both scaled to the squared value $B_c^2$ of the field at coil center:

$$F_1 = B_c^{-2} \left\langle \nabla B_x^2 + \nabla B_y^2 \right\rangle_{V_{OP}} \tag{9}$$

$$F_1' = B_c^{-2} \left\langle (\partial B_z/\partial z)^2 \right\rangle_{V_{OP}} \tag{10}$$

$F_1$ combines the squared gradients of the transverse components of $\mathbf{B}$ that are involved in the computation of the longitudinal relaxation rate $1/T_1$ :[7]

$$1/T_1 = DF_1, \tag{11}$$

where $D$ is the diffusion coefficient that depends on gas pressure $p$ as $Dp = 0.1914(T/300)^{1.71}$ mbar$\times$m$^2$/s ($T$ is the gas temperature in K).[5] In contrast, $F_1'$ averages squared derivatives with respect to $z$ in Eq. 10, and only those of $B_z$ which are not directly relevant for relaxation. However all components and their variations are linked by Maxwell's Equations and $F_1'$ is expected to be a relevant indicator for the minimisation of $1/T_1$ in $V_{OP}$, at least for axisymmetric configurations. In practice, the averages in

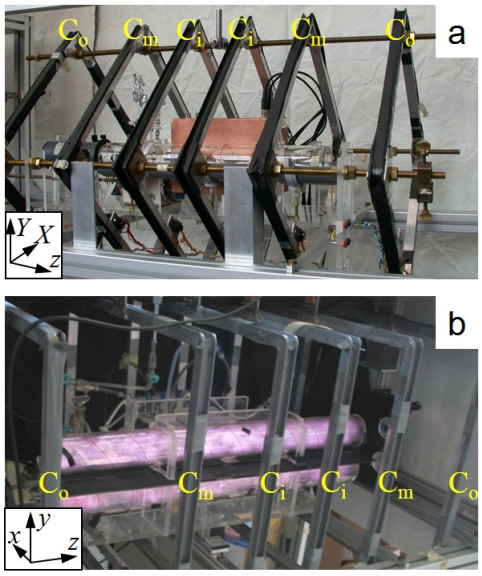


Figure 3: Side views of assembled sets of coils comprising six square coils in aluminum frames labelled according to Fig. 1c, containing OP cells consisting of a single (a) or a double (b) glass cylindrical volume. The RF discharge used for MEOP is active in Fig. b only.

Eqs. 9 or 10 are performed by computing $\mathbf{B}$-values at 50 $z$-locations regularly spaced on half of the axis of $V_{OP}$ ($z \geq 0$). The volume average for $F_1$ is evaluated from values every cm in the transverse directions whereas that of $F_1'$ only uses finite differences between adjacent $z$-locations on the axis of $V_{OP}$, which makes its computation much faster than that of all derivatives on a 3D grid.

For the low gas pressures relevant in MEOP, fast gas diffusion within $V_{OP}$ enforces a uniform gas polarisation, and $1/T_1$ is the volume average of local values of $1/T_1(z)$ that are involved in Eq. 9. In the the storage volume $V_S$, the higher gas pressures automatically yields decreased diffusion and reduced relaxation rates of the uniform polarisation (Eq. 11), a rate usually slow enough for the targeted application. A different contribution to the cost function is therefore introduced: the volume average average of the squared deviation of $B_z$ from its average $\overline{B_z}$, also scaled to $B_c^2$ :

$$F_2 = B_c^{-2} \left\langle \left(B_z - \overline{B_z}\right)^2 \right\rangle_{V_S}. \tag{12}$$

$F_2$ quantifies the width of the distribution of Larmor frequencies during NMR precession and is therefore directly related to the signal half-life $T_2^*$ involved the signal-to-noise ratio of NMR measurements.[12] In practice, the average in Eq. 12 is computed over 1/4 of the spherical volume on a grid comprising 11 points along a diameter of $V_S$ ($z \geq 0$ and $Y$ or $y \geq 0$, 172 sites).

The optimisation of the coil parameters is achieved by minimisation of a cost function combining $F_1$ or $F_1'$ and

$F_2$:

$$F = (F_1 + f_{21}F_2 + F_{\rm add})^{1/2}, \quad (13)$$

$$F' = (F_1' + f_{21}F_2 + F_{\rm add})^{1/2} \quad (14)$$

where $f_{21}$ is a parameter used to control the balance in required field homogeneity between OP and storage volumes, and $F_{\rm add}$ introduces additional terms that increase rapidly when targeted geometrical constraints are not met (the coils should not overlap, $d_{\rm o}$ should not exceed a set value, ...). The minimisation of the total cost function $F$ or $F'$ is numerically achieved using the robust downhill simplex method [13] implemented in the amoeba routine of Ref.[14] As is usual in minimisation protocols, the choice of a suitable initial set of parameters and of their probed variations (here, 20%) is important to avoid possible local minima and efficiently reach the solution. Attempts from different starting points and restarts from endpoints are used to ensure good convergence. Successive steps are actually performed to accelerate convergence to an optimal configuration.

As a first step, a coarse approximation of the windings by single current loops ($n = p = 1$) is made. Aluminum alloy frames made from welded U-profile (20×20×20×2 mm) are used for the sets of coils in Fig. 3. The windings within these frames are arranged in 1-mm-thick layers of 16 turns with a maximum of 16 layers to fill the winding volume. The same wire gauge and winding parameters are assumed for computations of six-coil sets throughout this article. A number of turns $N_{\rm o} = 224$ (14 layers) for the outer pair of coils is chosen at this stage since it approximately fills 90% of the winding volume. The minimisation of $F$ or $F'$ is performed for chosen geometrical constraints (size of coils, size and positions of volumes $V_{\rm OP}$ and $V_{\rm S}$) and for a fixed value of $f_{21}$ in Eq. 13 or 14. The corresponding optimal set of parameters ($d_i$ and $N_i$) is used to compute illustrative 2D field maps and to evaluate the values of $T_1$ in $V_{\rm OP}$ and $T_2^*$ in $V_{\rm S}$. The full expression $F_1$ of Eq. 9 is used to evaluate $T_1$ even when $F'$ is used for the optimisation. Visual inspection of the field maps is used to qualitatively assess the field homogeneity while the comparison of the relaxation rates with targeted upper bounds for these rates is used to choose the weight $f_{21}$ given to field inhomogeneities over $V_{\rm S}$ in the minimised function $F$ or $F'$, as shown on an example in Section 3.2. At the end of the process, it can be concluded whether a configuration with coils of a set size ($L_{\rm min}$, maximum $d_{\rm o}$) can yield a satisfactory field homogeneity over the chosen OP and storage volumes.

The second optimisation step consists in replacing the single current loops with discrete lattices of currents (Fig. 1b) and therefore computing more realistic field maps, optimal coil positions, and ratios of numbers of turns ($N_{\rm i}/N_{\rm o}$, $N_{\rm m}/N_{\rm o}$).

The third step consists in finding three integer numbers of turns with ratios closely approximating the optimal ratios found in the second step, and performing the optimisation of the three coil positions for these fixed numbers of turns. This set of parameters is used for the construction of the coil frames, and the actual dimensions of the coil windings are used for a final optimisation of the coil positions. Small variations of geometric parameters can also be used at this stage to probe the sensitivity of field maps to construction or winding imperfections. For instance, variations of one coil pair spacing $d_k$ by ±2 mm typically shortens $T_1$ by less than 10%.

# 3 Results

## 3.1 On-axis optimisation

The results displayed in Fig. 4 illustrate the differences in optimal parameters and resulting field maps for similar coils systems designed using the target-oriented numerical optimisation reported in this article or using an analytical method.[10]

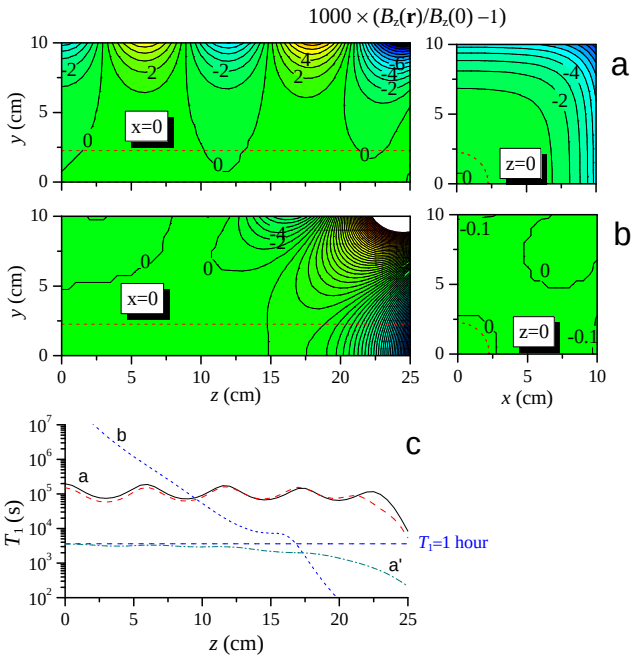


Figure 4: Computed field maps (a and b) and associated relaxation times (c) for sets of six square coils of equal side lengths $L = 0.4$ m, with positions and numbers of turns listed in Table 1. Maps and curves a: results of on-axis optimisation over an extended cell volume. b: results for the analytically derived coil parameters of Ref. [10] The maps of $B_z(\mathbf{r})/B_z(0) - 1$ are displayed in one quadrant of vertical planes (with contours every 0.1%). The dashed lines in the maps mark the on-axis location of $V_{\rm OP}$. c: computed variations of local $T_1$ with $z$ for $^3$He gas at $p = 0.4$ mbar. Curves a are obtained for maps minimising $F_1$ (solid black line) or $F_1'$ (dashed red line). Curve a′ is the local $T_1$ (in field map a) for the off-axis OP volume of Fig. 2a. Curve b is the on-axis local $T_1$ for the field map of Ref. [10]

Here, in contrast with coil systems designed to ac-

commodate an OP cell and a storage cell (Fig. 2 and Refs.[4, 5]), the coil parameters are varied to only minimise $F_1$ over an OP cell centred on the $z$-axis. This solution can be of interest for various applications, and can be directly compared to that proposed in Ref. [10] More precisely, the 'wire coils' parameters in Table 1 and the maps in Fig. 4a are obtained for sets of current loops having the same side length as those of Ref. [10] The optimal ratios

| system | $d_i$, $d_m$, $d_o$ (cm) | $N_i$, $N_m$, $N_o$ (turns) | $B_z(0)/I$ (mT/A) |
|---|---|---|---|
| Wire coils | 6.03, 18.50, 35.41 | 84, 93, 189 | 0.825 |
| Real coils | 5.93, 18.14, 34.96 | 87, 95, 204 | 0.877 |
| Ref. [10] | 3.66, 12.20, 27.34 | 57, 78, 200 | 0.888 |

Table 1: Optimised coil positions, number of turns, and computed field at coil centre for three configurations of coil sets. The first two lines minimise $F_1$ (Eq. 9) for a 25-cm-long cell centred on the $z$-axis, for single current loops (Wire coils) or realistic extended windings (Real coils). The Wire coils system is given for direct comparison with the coil system of Ref. [10] (third line).

found in that case ($N_i/N_o = 0.4447$, $N_m/N_o = 0.4917$) yield minimal rounding errors for $N_o = 189$ and the final parameters in the first line of Table 1. The field maps of the two systems plotted in Figs. 4a and 4b exhibit features associated with their optimisation approaches: field deviations within 10 cm from the coil centre are much weaker in Fig. 4b (note that contour lines are drawn every $10^{-4}$ for the transverse plane map, every $10^{-3}$ for the other maps). But, as expected, field deviations remain moderate further away from the coil centre (between $z = 10$ cm and $z = 25$ cm) only in Fig. 4a. As a result, the values of $z$-dependent magnetic relaxation time in Fig. 4c, computed for a 5-cm-diameter OP cell, remain safely long enough for efficient MEOP over the whole plotted range of $z$ only for the suitably designed system (solid curve labelled a): in that case, $T_1$ exceeds 1 hour at the lower end of the gas pressure range used for efficient MEOP.[1] The differences in system parameters and in the corresponding variations of $T_1$ with $z$ obtained by minimisation of $F_1$ or $F_1'$ are very small, as could be expected for an OP volume close to the axis of symmetry of the system. Figure 4c also displays the variation of $T_1$ in an off-axis OP volume. All variations of $T_1$ correlate well with the displayed field maps.

The smaller of the sets of six square coils used in gas polarising systems (Fig. 2a) has an average side length of order 0.4 m, the same as that of the coil systems compared in Fig. 4. The second optimisation step starting from the wire coil solution in Table 1 is therefore performed for realistic winding sizes, yielding the configuration given for 'Real coils' in Table 1. The optimal coil positions are only slightly affected, but larger modifications in the numbers of turns (in the ratios $N_i/N_o = 0.4265$, $N_m/N_o = 0.4657$) are found with respect to the optimised wire coils. However, the differences (not shown) in field maps and in $z$-dependent relaxation times are very small. An alternative solution for $N_o = 176$ also yields very similar field and $T_1$ maps.

## 3.2 Off-axis optimisation

For gas polarising systems, the joint optimisation of field maps over the off-axis OP and storage volumes instead of the on-axis optimisation achieved in Section 3.1 starts with series of coarse calculations: the first minimisation step mentioned at the end of Sect. 2.2, with $n = p = 1$ and non-integer numbers of turns. For fixed coil size as well as OP and storage volumes and locations, the influence of the choice of the parameter $f_{21}$ in Eq. 9 or 10 on the performance of the optimised coil system is first assessed. Figure 5 displays the corresponding results for the relaxation time $T_1$ in the OP cell and the NMR decoherence time $T_2^*$ in the storage volume of the larger coil system (Fig. 2b). In addition, the outcomes of minimisations based on the use of $F$ or $F'$ are compared (solid or open symbols, respectively). With both approaches, joint decreases in $T_1$ and increases in $T_2^*$ with $f_{21}$ are found, but the use of $F'$ for computations which are typically ten times faster should not be trusted to yield reliably optimised configurations for off-axis OP and storage volumes. Figure 5 also indicates that choosing $f_{21}$ of the order of 1 yields satisfactory values $T_1 \approx 1700$ s and $T_2^* \approx 3$ s for this coil system. The same study for the smaller coil system of Fig. 2a yields similar variations of $T_1$ and $T_2^*$ with $f_{21}$, but with values typically 1.5–2.5 times shorter than those obtained for the larger system.

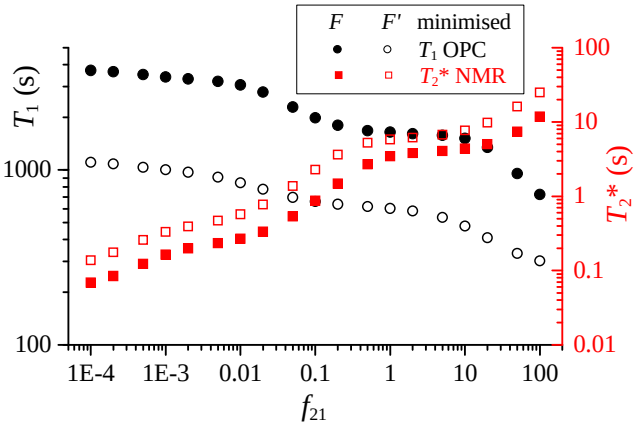


Figure 5: Computed global $T_1$ in $V_{OP}$ (for $p = 0.4$ mbar) and $T_2^*$ in $V_S$ (for a Larmor frequency of 40 kHz, typical of actual systems) obtained for the system of Fig. 2b when minimising $F$ or $F'$ (see legend). The parameter $f_{21}$ sets the relative weight of inhomogeneities in the minimisation process (Eqs. 13 and 14).

The next optimisation steps for the two configurations of Fig. 2 yields parameters and associated field maps which significantly differ from the results of on-axis optimisations. Sets of optimised parameters are listed in

Table 2 (for arbitrary numbers of turns) and the first part of Table 3 (for integer numbers of turns, sets a and b), corresponding to minimisations of the cost function $F$ of Eq. 13 with $f_{21} = 1$.

| set | $L_{\min}$ (cm) | $d_i$, $d_m$, $d_o$ (cm) | $N_i/N_o$, $N_m/N_o$ | $1/T_1$ ($h^{-1}$) |
|---|---|---|---|---|
| a | 38.4 | 4.90, 16.47, 33.26 | 0.3661, 0.4825 | 5.38 |
| b | 50.4 | 6.52, 21.88, 43.75 | 0.3767, 0.4894 | 2.17 |

Table 2: Optimised coil positions, ratios of numbers of turns, and averaged relaxation rates in $V_{OP}$ for $p$ = 0.4 mbar (the corresponding averaged relative gradients from Eq. 11 are $5.6 \times 10^{-4}$ and $3.6 \times 10^{-4}$ $cm^{-1}$ for sets a and b). Results are obtained minimising the cost function $F$ for the coil sets of Fig. 2 assuming $N_o = 224$.

Corresponding maps of field inhomogeneities are displayed in Figs. 6a and b, onto which the off-axis locations of the relevant volumes for the optimisations are marked. The $z$-dependent local $T_1$ values in the OP volumes are

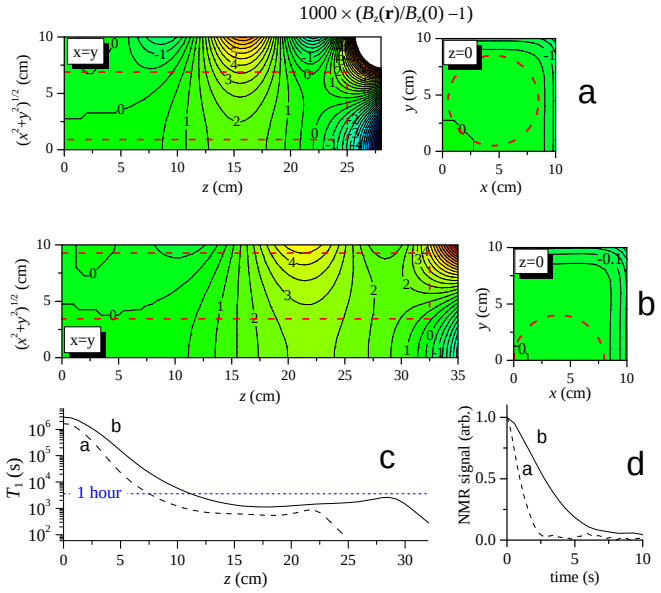


Figure 6: Computed field maps for the smaller (a) and larger (b) set of coils of Table 3, with contour lines every 0.1% (0.01% in the plane $z = 0$ of b). The dashed lines in the maps mark the locations of $V_{OP}$ in the diagonal planes $x = y$ and of $V_S$ in the planes $z = 0$. c: Variations of local $T_1$ in $V_{OP}$ for $p = 0.4$ mbar. d: NMR signal decays in $V_S$ at 40 kHz.

displayed in Fig. 6c. The computed decoherence of precessing magnetisation within $V_S$ (Fig. 6d) yields signal half-lifes of the order of 1 and 3 s .

The second part of Table 3 (sets a′ and b′) lists the parameters used for the construction of the experimental systems depicted in Fig. 3. They were obtained by minimising the cost function $F'$ of Eq. 14, before the quantitative comparison summarised in Fig. 5 was performed,

| set | $L_{\min}$ (cm) | $d_i$, $d_m$, $d_o$ (cm) | $N_i$, $N_m$, $N_o$ (turns) | $B_z(0)/I$ (mT/A) |
|---|---|---|---|---|
| a | 38.4 | 4.90, 16.47, 33.25 | 82, 108, 224 | 0.973 |
| b | 50.4 | 6.54, 21.94, 43.83 | 90, 117, 239 | 0.798 |
| a′ | 38.4 | 5.90, 19.10, 37.80 | 85, 100, 224 | 0.852 |
| b′ | 50.4 | 6.17, 20.08, 40.74 | 80, 101, 221 | 0.759 |

Table 3: Sets a and b: Optimised coil positions and numbers of turns for the coil sets of Fig. 2 and computed field values at coil centre, obtained when minimising the cost function $F$. The corresponding field maps and data are plotted in Fig. 6. Sets a′ and b′: Parameters obtained when minimising $F'$, used for the experimental systems of Fig. 3. With resistance values of 27 and 37 Ω at room temperature for the coils sets a′ and b′, power dissipation factors of 37 and 67 W/mT$^2$ are inferred from $B/I$ data.

and therefore the performance of the actual coil systems is expected to be lower than that of the true optimum.

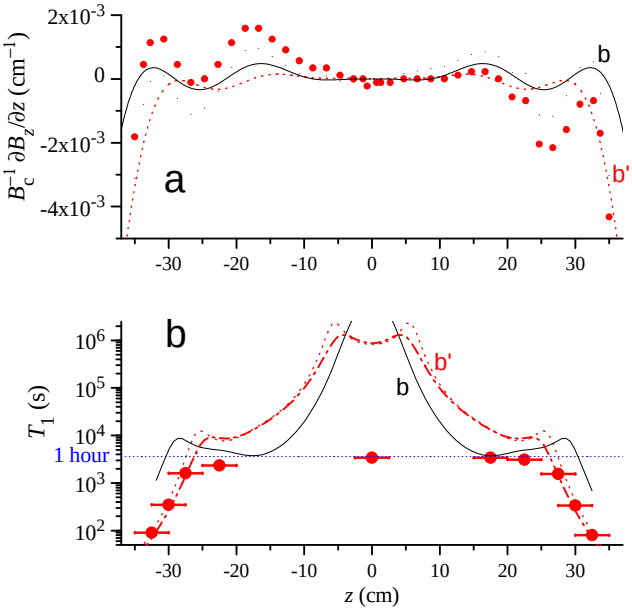


Figure 7: a: Computed axial field derivatives on the OP cell axis for the coil set parameters b and b′ of Table 3 (solid and dotted lines), and corresponding data inferred from $B_z$ measurements for currents $I = \pm 1$ A using a single-axis fluxgate magnetometer (Bartington MAG-01MS, ±1 mT). b: Computed $T_1(z)$ values within $V_{OP}$ for the coil sets b and b′ ($p$ = 1.33 mbar). The dash-dotted line and solid symbols are volume-averaged computed values and experimental results for a 4.5-cm-long (the length of the bars) probing cell (see text).

This is illustrated in Figs. 7a and b for the larger coil set of Fig. 3b: computed field $z$-derivatives on the axis of $V_{OP}$ and local values of $T_1$ are compared for coil sets b and b′ (solid and dotted lines) and to measured experimental data (solid symbols). The larger than expected oscilla-

tions and the asymmetry of measured data in Fig. 7a are attributed to construction and winding imperfections, but the rapid drop beyond $|z| = 35$ cm which is computed for the b′ coil set is clearly observed.

Experimental $T_1$ data in Fig. 7b were derived from NMR measurements performed at coil centre using a sealed pyrex glass cell (I.D. 4.5-cm, length 4.5 cm) filled with 1.33 mbar of MEOP-polarised $^3$He gas. FID signal ratios for $\pi/4 - \Delta t - \pi/2$ pulse pairs were used for various dwell times $\Delta t$ spent at different positions $z$. $T_1$ values were limited by wall relaxation over most of the explored range of $z$ (1 hour is typical for pyrex glass with such surface-to-volume ratio), and steeply decreased beyond $|z| = 28$ cm, in good agreement with the expected harmonic averages of computed $T_1(z)$ over the length of the probing cell. Computations and experimental checks agree well, and show that performing full optimisation with the more relevant cost function $F$ would have led to a better experimental system, suitable for longer OP volumes with acceptable relaxation losses.

### 3.3 Control of transverse field components

So far, only the need to apply an axial $B_z$ field has been considered, but transverse field components may play an important role in various situations. For MEOP, the magnetic field applied on optically pumped atoms must be collinear with the the circularly polarised OP light beam, and in long cells this can be achieved only if the transverse field components (due, for instance, to the Earth's field $\mathbf{B}^{\mathrm{E}}$) are negligible compared to $B_z$. Below a few mT this may require compensating these components without introducing significant additional inhomogeneities in the total field $\mathbf{B}$. In other situations, one may wish to deliberately vary the relative orientation of pump or probe light beams with respect to the magnetic field,[15] and it is convenient to operate with fixed cell and light beams orientations and use additional sets of coils generating uniform fields along the transverse directions $B_x$ and $B_y$ as well.

Figure 8 shows the full set of coils used in the experiments of Ref. [15] The six square coils, arranged as discussed in Sect. 3.1 or 3.2 depending on the targeted $B_z$ map, are assembled by brass threaded rods near their corners as in Fig. 3a. The transverse field components are generated by two pairs of rectangular coils comprising 40 turns each. They are wound inside $20\times20$ mm$^2$ PVC wireways assembled using plastic angle brackets. Their outside widths just fit inside the 36-cm clearance of the $B_z$ coils to which they are attached. Their outside lengths are similar to the length of the $B_z$ coil set, with the $B_x$ coil pair fitting inside the longer $B_y$ coil pair. In many locations worldwide the largest of the Earth's field component is vertical, and the $z$-axis may in addition be coarsely aligned with Earth's field horizontal component. The required compensating $B_y$ field is therefore usually larger than the compensating $B_x$ field and the longer coil pair, that generates a slightly more uniform field, is used for $B_y$.

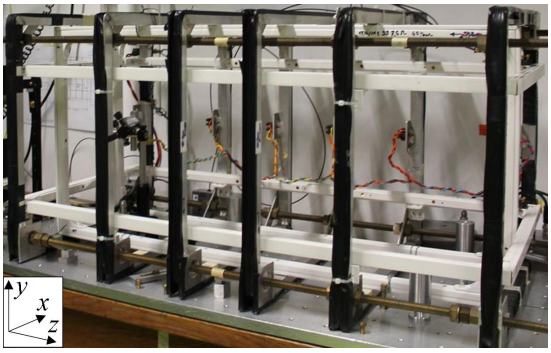


Figure 8: View of an assembled set of magnetic field coils comprising six square coils in aluminum frames (for $B_z$) and two pairs of rectangular coils in white PVC wireways (for $B_x$ and $B_y$).

Selected computed field maps of $B_y$ inhomogeneities are displayed in Fig. 9a for average coil positions $d_y = \pm10$ cm. Note that the typical deviations are one order of magnitude larger than for the six-coil sets (Figs. 4 and 6). The maps of $\nabla B_x$ and $\nabla B_y$ (relevant for relaxation in the net $B_z$ field) that are due to the compensating $-B_y^{\mathrm{E}}$ field are computed and used to infer $T_1(z)$ (Fig. 9b) for a 4.5-cm-diameter OP volume centred on the $z$-axis. More precisely, $T_1$ is the product of the displayed data by $(B_z/B_y^{\mathrm{E}})^2$, assuming a negligible contribution to relaxation of the field gradients due to the six-coil set used for $B_z$. No $N$-dimensional optimisation is performed to design these compensation coils, and a comparison of the $T_1$ data computed for different coil separations shows an optimal value $2d_y = 20$ cm. The field maps of the shorter coil pair used for $B_x$ (72.5-cm-long, not shown) are hardly less uniform and yield similar $T_1(z)$ results. The fields generated by these compensation coils are $B_y = 0.154$ mT/A and $B_x = 0.156$ mT/A. The two data points in Fig. 9b correspond to relaxation in the same cell as for Fig. 7b. The increase in relaxation rates when $-B_x^{\mathrm{E}} = 15$ $\mu$T and $-B_y^{\mathrm{E}} = 34$ $\mu$T are applied was measured using optical detection of polarisation at several cell positions for values of $B_z$ ranging from 10 to 200 $\mu$T.

## 4 Discussion

The pragmatic and target-oriented design approach described in this article yields compact coil systems with relative field inhomogeneities at the per mil level over extended and elongated volumes. They are simpler to construct and provide better experimental access than end-compensated solenoids. The typical usable length for OP cells, either on-axis or off-axis, is found to be $\simeq 1.15 \times L$ (the common coil side length), which is 60% longer than is analytically designed similar coil systems (Ref. [10], see

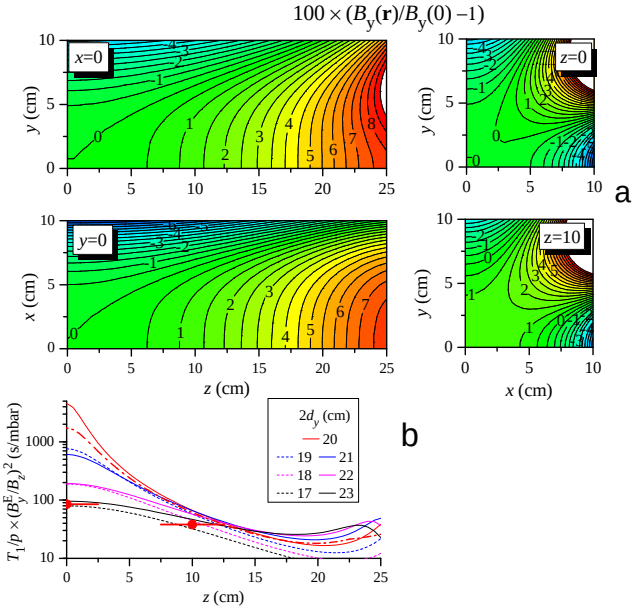


Figure 9: a: Computed field maps for the rectangular $B_y$ coil pair, with wire dimensions 77 cm × 34.5 cm and mean separation 20 cm. The maps of $B_y(\mathbf{r})/B_y(0) - 1$ are displayed in one quadrant of horizontal and vertical planes including the $z$-axis and of vertical planes at the coil centre and 10 cm away (contours every 0.5% in all plots). b: Local relaxation times in $V_{\rm OP}$ for $p = 1$ mbar (see text) for various coil separations $2d_y$ (see legend). The dash-dotted line and solid symbols are volume-averaged computed values and experimental results for a 4.5-cm-long (the length of the bars) probing cell and $2d_y = 20$ cm.

Sec. 3.1) while the typical coil set length is $\simeq 1.7 \times L$.

One important parameter characterising the quality of the coil system is the relaxation time $T_1$ in the OP volume. The variations with $z$ of the local $T_1$ plotted for various coil systems can be used to assess the dominant location of relaxation losses which may affect MEOP efficiency, and the maximum OP cell dimensions one may use in a given system. For instance, the comparison of Figs. 4c and 6c which correspond to different optimisation objectives (on-axis minimisation of $F_1$ versus off-axis joint minimisation of $F_1$ and $F_2$), illustrates that the sole minimisation of $F_1$ yields a more uniform $T_1(z)$ both on- and off-axis and therefore a longer overall $T_1$ (1430 s vs. 670 s). This difference arises from the added constraint on $F_2$ for Fig. 6c, that is from the higher field uniformity requested at small $z$ in $V_{\rm S}$ which results in poorer uniformity at larger $z$. In that case, the balance in the values achieved for $T_1$ and $T_2^*$, that are both suitable for the targeted application of such coil systems, results from the choice $f_{21} = 1$ made for these optimisations.

As regards the simple coil pairs of Sect. 3.3 used to control transverse field components, and in particular compensate those of the Earth's field, the influence of their computed inhomogeneities on $T_1(z)$ is found to critically depend both on the operating $B_z$ field value and on the length of $V_{\rm OP}$. The experimental $T_1(z)$ data induced by field inhomogeneities of these coil pairs are found to be significantly shorter than computed, in contrast to the good agreement obtained for the main field of the six-coil sets. This is attributed to the imprecise positioning of the windings in rather flexible wireways and a more rigid construction is expected to reduce relaxation losses in the vicinity of the coil centre. Further improvement may be obtained using an approach similar to that used for optimisation of the six-coil sets and computing field maps for optimised sets of two pairs of rectangular coils, instead of one, for each of the transverse directions. Details fall beyond the scope of this article, and the solution was not experimentally tested, but typical improvement on achievable $T_1$s by a factor 10 is obtained for sets of four rectangular coils with the same size as those of the compensating pairs.

More generally, the design method relying on the minimisation of numerically computed cost functions of field maps for sets of coils consisting of straight current elements can be advantageously used in situations where a mere cancellation of coefficients in a Taylor expansion does not offer sufficient control to achieve a specific objective. This approach was for instance found to be efficient in the design of different kinds of low-frequency RF coils used in NMR experiments.[16] Similar approaches involving field computations over an extended volume can be found in the literature, but they use a rather unspecific cost function for rotationally invariant coil system and field optimisation volume[17] or they involve a simple rms field deviation and very heavy finite element method simulations.[12] Quite generally, defining a suitable cost function specifically tailored to achieving targeted system performance – here, a satisfactory balance of $T_1$ and $T_2^*$ for gas in different volumes – may a key step in the design of optimal systems.

## Acknowledgments

Contributions of Cavin Talbot and Tangi Baré to characterisations of experimental systems are gratefully acknowledged.

# References

[1] T. R. Gentile, P. J. Nacher, B. Saam, and T. G. Walker. 'Optically polarized $^3$He.' *Rev. Mod. Phys.*, 89:045004 (2017).

[2] C. Mrozik, O. Endner, C. Hauke, W. Heil, et al. 'Construction of a compact $^3$He polarizing facility.' *J. Phys. Conf. Ser.*, 294:012007 (2011).

[3] T. R. Gentile, D. R. Rich, A. K. Thompson, W. M. Snow, et al. 'Compressing spin-polarized He-3 with a modified diaphragm pump.' *J. Res. Nat. Inst. Stand. Technol.*, 106(4):709–729 (2001).

[4] J. Choukeife, X. Maitre, G. Tastevin, and P.-J. Nacher. 'On-site production of hyperpolarised helium-3 gas for lung MRI.' *Proc. Int. Soc. Magn. Reson. Med.*, page 1391 (2003).

[5] G. Tastevin and P.-J. Nacher. 'NMR measurements of hyperpolarized He3 gas diffusion in high porosity silica aerogels.' *J. Chem. Phys.*, 123:064506 (2005).

[6] D. S. Hussey, D. R. Rich, A. S. Belov, X. Tong, et al. 'Polarized He-3 gas compression system using metastability-exchange optical pumping.' *Rev. Sci. Instrum.*, 76(5):053503 (2005).

[7] G. D. Cates, S. R. Schaefer, and W. Happer. 'Relaxation of spins due to field inhomogeneities in gaseous samples at low magnetic fields and low pressures.' *Phys. Rev. A*, 37:2877–2885 (1988).

[8] R. Merritt, C. Purcell, and G. Stroink. 'Uniform magnetic field produced by three, four, and five square coils.' *Rev. Sci. Instrum.*, 54:879–882 (1983).

[9] W. Franzen. 'Generation of uniform magnetic fields by means of air-core coils.' *Rev. Sci. Instrum.*, 33:933 (1962).

[10] W.-Z. Wang, B.-T. Hu, H. Zheng, X.-Q. Tu, et al. 'A new magnetic field system for He-3 polarization.' *Acta Physica Sinica*, 67:1 (2018).

[11] Y. Huang, L. Jiang, P. Fu, Z. Huang, et al. 'Optimal design method to improve the magnetic field distribution of multiple square coil systems.' *IEEE Access*, 8:171184–171194 (2020).

[12] T. Liu, A. Schnabel, J. Voigt, W. Kilian, et al. 'A built-in coil system attached to the inside walls of a magnetically shielded room for generating an ultra-high magnetic field homogeneity.' *Rev. Sci. Instrum.*, 92(2):024709 (2021).

[13] J. Nelder and R. Mead. 'A simplex method for function minimization.' *The computer journal*, 7(4):308–313 (1965).

[14] W. Press, W. Vetterling, S. Teukolsky, and B. Flannery. *Numerical Recipes in FORTRAN.* Cambridge University Press, London, UK (1988). ISBN 9780521430647.

[15] A. Dia, M. Abboud, P.-J. Nacher, and G. Tastevin. 'Doppler-free spectroscopy of the lowest triplet states of helium using double optical resonance.' *Eur. Phys. J. D*, 75(8):223 (2021).

[16] P.-J. Nacher, S. Kumaragamage, G. Tastevin, and C. Bidinosti. 'A fast MOSFET rf switch for low-field NMR and MRI.' *J. Magn. Reson.*, 310:106638 (2020).

[17] A. E. Krosney, M. Lang, J. J. Weirathmueller, and C. P. Bidinosti. 'Magnetic diffusion, inductive shielding, and the Laplace transform.' *Am. J. Phys*, 89(5):490–499 (2021).